MNRAS **000**, 1–12 (2019) Preprint 19 October 2020 Compiled using MNRAS LATEX style file v3.0

Space observations of AA Doradus provide consistent mass determinations

A.S. Baran,[1,2]★ R.H. Østensen,[1,2,3] U. Heber,[4] A. Irrgang,[4] S. Sanjayan,[1,5] M.D. Reed,[1,2] J. Ostrowski,[1]

[1]*ARDASTELLA Research Group, Institute of Physics, Pedagogical University of Krakow, ul. Podchorążych 2, 30-084 Kraków, Poland*
[2]*Department of Physics, Astronomy, and Materials Science, Missouri State University, Springfield, MO 65897, USA*
[3]*Recogito AS, Storgaten 72, N-8200 Fauske, Norway*
[4]*Dr. Karl Remeis-Observatory & ECAP, Astronomical Institute, Friedrich-Alexander University Erlangen-Nuremberg (FAU), Sternwartstr. 7, 96049 Bamberg, Germany*
[5]*Centrum Astronomiczne im. Mikołaja Kopernika, Polskiej Akademii Nauk, ul. Bartycka 18, 00-716 Warszawa, Polska*

Accepted XXX. Received YYY; in original form ZZZ

ABSTRACT

We present a detailed analysis of the properties of AA Dor based on new space observations. This sdOB+dM binary has recently been monitored for almost a full year with the *TESS* satellite, providing an excellent time-series dataset to search for stellar pulsations and eclipse timing variations. Additionally, we used the high-precision trigonometric parallax from Gaia to make an independent determination of the fundamental stellar parameters. No pulsations were detected down to a limit of 70 parts per million. From eclipse timing measurements we were able to confirm that the orbital period is stable, with an upper limit to any period change of $5.75{\cdot}10^{-13}$ s/s. The apparent offset of the secondary eclipse is consistent with the predicted Rømer delay when the primary mass is that of a canonical extended horizontal branch star. Using parallax and a spectral energy distribution corroborates that the mass of the primary in AA Dor is canonical, and its radius and luminosity is consistent with an evolutionary state beyond core helium burning. The mass of the secondary is found to be at the limit of hydrogen burning.

Key words: binaries: general subdwarfs, stars: oscillations (including pulsations), stars: eclipsing binaries, stars: individual (AA Dor)

1 INTRODUCTION

Subdwarf B (sdB) stars are identified as compact stars located on the blue extension of the horizontal branch (EHB). The progenitors of sdB stars are intermediate-mass stars like the Sun that must have lost significant mass during or immediately after their ascent of the red-giant branch, leaving them with only a tiny remnant of their hydrogen envelopes. The mass loss must happen before helium ignition, otherwise they would become normal horizontal branch stars (Heber 2016). Binary population synthesis modelling have been performed exploring various mass-loss scenarios, as detailed by Han et al. (2002). Several channels exist, depending on the initial configuration of the system, and depending on the mass ratio, the binary system ends up either in a wide orbit (via stable Roche-lobe overflow, when the companion is sufficiently massive) or a close orbit (after common-envelope ejection, when the companion is of lower mass than the stripped EHB star). Since EHB stars must have a mass close to the core-helium flash mass of $0.5\,M_{\odot}$, the close-orbit systems can only consist of an sdB with either an M dwarf (dM), brown dwarf, or white dwarf companion.

HW Vir is the class prototype for the sdB+dM systems (Menzies & Marang 1986). Wolz et al. (2018) provided a list of all HW Vir systems studied prior to 2018. It contains 20 systems including those with brown dwarfs as secondaries. A large number of faint HW Vir candidates from ground-based photometric surveys was recently published by Schaffenroth et al. (2019). A typical light curve of HW Vir systems shows two distinct eclipses and an out-of-eclipse variation, explained by an irradiation effect. The eclipses indicate a nearly edge-on orbital orientation (inclination close to 90°). Eclipse mid-times can be used to study the stability of the orbital period, sometimes leading to the discovery of periodic modulations in the eclipse timings, which is indicative of additional companions (e.g. Baran et al. 2015).

HW Vir systems are important objects for testing the proposed evolutionary channels of sdB stars described by Han et al. (2002). Deriving the masses of both components is therefore crucial, but difficult. HW Vir systems are usually single-lined spectroscopic binaries, since the secondary companions are not easily detectable in the presence of the more luminous hot stars. The luminosity ratio is

★ E-mail: andrzej.baran@up.krakow.pl

© 2019 The Authors

of the order of 10^6. Masses of sdB stars are frequently assumed to be close to $0.47M_\odot$ (Fontaine et al. 2012), which is often referred to as the canonical mass. In fact, a narrow range of helium core masses is typical for a wide mass range of progenitors ($0.7–1.9M_\odot$) that undergo a helium flash. The canonical mass of about $0.47M_\odot$ is the flash mass for solar metallicity. With a wide range of metallicities, the permitted range for the core-helium flash extends to between 0.43 and 0.5 $M_\odot$ (Dorman et al. 1993). However, there is also the chance that an sdB's mass could be down to 0.31 $M_\odot$, produced by a narrow range of progenitor masses close to 1.9–2.2 $M_\odot$, and for a wider range (2.2–3.7 $M_\odot$) of progenitors that ignite helium under non-degenerate conditions. Thus, for any particular HW Vir-type system, while a canonical mass for the primary is most likely, it is dangerous to make this a general assumption as it may lead to incorrect conclusions about other system parameters.

Stellar oscillations predicted and discovered in sdB stars by Charpinet et al. (1997) and Kilkenny et al. (1997), respectively, are potentially useful for sdB mass estimations. Asteroseismology uses pulsation properties to describe stellar interiors, with a recent example of a mass estimation given by Charpinet et al. (2019). Surprisingly, the estimated mass is $0.39M_\odot$, which is significantly below the canonical mass. Other derived masses have been closer to the canonical one, (see for example Charpinet et al. 2011; Baran et al. 2019). To date, the sample of pulsating sdB stars is approaching a hundred, with half of the sample discovered during the space photometry missions *Kepler*, *K2* and *TESS*.

Binary systems provide an independent tool to estimate masses. In the case of HW Vir systems, the masses are not easily derived, since a significant temperature difference between components makes it difficult to see the secondary/fainter companion and typically the mass estimation for the secondary is based on an assumption of the primary having the canonical mass, which may not always be correct. Kaplan (2010) reported of a new tool to estimate masses in binary systems. He showed that, even in the case of a circular orbit, a secondary eclipse is not centered at 0.5 orbital phase, but is observed with a lag, also known as the Rømer delay. The predicted delay may be just a few seconds, and therefore very precise data are required. Barlow et al. (2012) measured that shift in 2M 1938+4603, one of the systems observed by the *Kepler* spacecraft. They measured the delay to be below 2 s and consequently the mass of the primary to be $0.37M_\odot$. Next, Baran et al. (2015) used a longer time span and arrived at a slightly smaller shift. These authors reported the mass of the secondary to be smaller than $0.3M_\odot$, which is contrary to the canonical mass. However, both Barlow et al. (2012) and Baran et al. (2015) noted that the eccentricity of the orbit may also contribute to the offset of the secondary eclipse and the overall shift may not be purely caused by the Rømer delay. In that case, the mass estimation may not be correct. Baran et al. (2018) reported an attempt to apply the Rømer-delay method to HW Vir. The mass the authors derived was similar to that of 2M 1938+4603. They also arrived at the same conclusion about eccentricity, but noted that when the radii of the stars are large in relation to the orbital separation, several geometric effects can contribute to reduce the observed Rømer delay. Together these cases showed that the idea of Kaplan (2010) is very tough to employ conclusively, especially since it is impossible to observe eccentricity to the precision required for reasonably precise mass derivations. A mass as low as $0.3M_\odot$ can only be reconciled with evolutionary models if the hot subdwarf fails to ignite helium and evolves from the RGB directly to the white dwarf cooling track, in what is known as post-RGB systems.

2M 1938+4603 and HW Vir were observed during the *Kepler* mission, which provided continuous time-series data of unprecedented quality. These were good enough to estimate the shift of the secondary eclipse. Another HW Vir-like system observed during a space mission is AA Dor, which is located in the southern continuous viewing zone of the *TESS* satellite. A flux variation of AA Dor was first reported by Kilkenny & Hill (1975) and this system has since been studied regularly. The light curve of AA Dor resembles that of HW Vir though because the estimated mass of the fainter component falls below the hydrogen core burning stellar configuration, the secondary was considered to be a brown dwarf. The relatively high effective temperature and surface gravity places the AA Dor primary above the regular EHB region in the Kiel diagram, which means that if its mass is canonical, it must have evolved beyond the core-helium-burning stage to the post-EHB shell-helium-burning stage. In this respect it is similar to V1828 Aql (=NSVS 14256825 Almeida et al. 2012) and EPIC 216747137 (Silvotti et al. 2021, submitted).

To determine stellar masses reliably one needs to detect spectral lines of both components. A spectroscopic effort to determine the nature of the secondary component was undertaken *e.g.* by Hilditch et al. (1996) and Rauch & Werner (2003). No definite conclusion has been achieved, since the mass of the primary had to be assumed upfront. Vučković et al. (2008) re-analyzed the spectroscopic data of Rauch & Werner (2003), discovering emission lines originating from the heated side of the secondary. The authors made the first estimate of the masses of both AA Dor components, which were consistent with a regular EHB primary and a low-mass M dwarf secondary. A subsequent effort by Klepp & Rauch (2011a) ruled out the post-RGB channel. Updated work by Hoyer et al. (2015) and Vučković et al. (2016) produced the best estimations of radial velocity amplitudes of both components, allowing for precise mass determinations of both components. Both authors cited radial velocity amplitudes and corresponding masses that agree, within the errors, though the uncertainty of the radial velocity amplitude of the secondary component reported by Vučković et al. (2016) is an order of magnitude smaller. The masses indicate that the primary star is close to canonical, and the secondary is on the limit of hydrogen burning for a main sequence star.

In this paper we describe the *TESS* data in Section 2, search for pulsations in Section 3 and explore eclipse timings in Section 4. We report results of our work using *TESS* data of AA Dor in Section 5, in which we estimate masses of both components. In Section 6 we explore another method to derive the fundamental stellar parameters using published atmospheric parameters, modelling the spectral energy distribution and making use of the high-precision trigonometric parallax provided by the second data release of *G*aia.

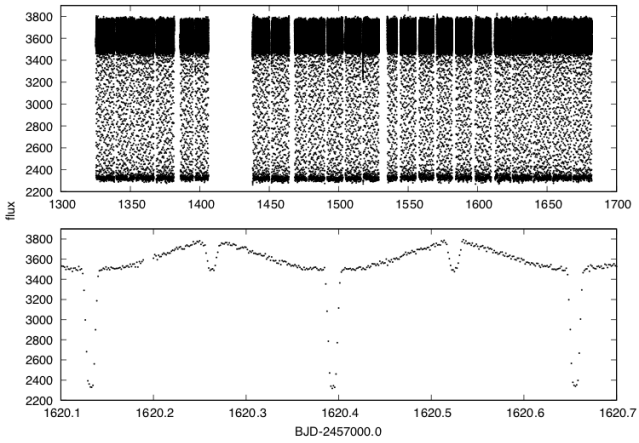

Figure 1. Light curve of AA Dor obtained by *TESS* during Year 1 of the mission. The top panel shows the entire processed data set, while the bottom panel shows the flux variations during a couple of orbital periods.

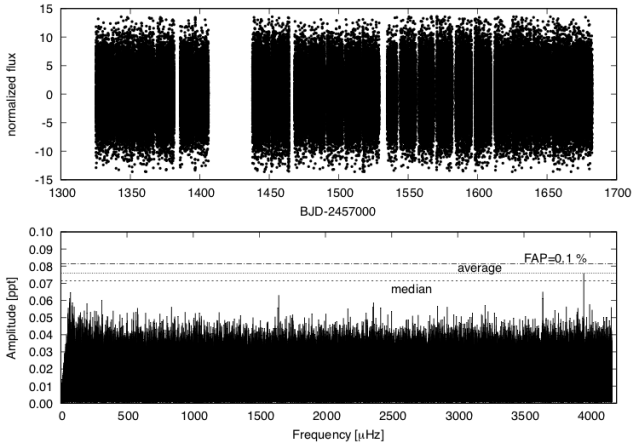

Figure 2. Top panel: residuals of prewhitening and clipping. Bottom panel: amplitude spectrum up to the Nyquist frequency (4166 μHz). The dashed and dotted lines in the bottom panel represent S/N = 5 calculated using median (0.0714 ppt) and average (0.0761 ppt), respectively. The dashed-dotted line represents FAP = 0.1%.

2 TESS PHOTOMETRIC DATA

AA Dor (α_{2000} = 05$^{\rm h}$31$^{\rm m}$40.36$^{\rm s}$, δ_{2000} = −69°53′02.2″) was observed during the first cycle of the nearly all-sky survey undertaken with the Transiting Exoplanet Survey Satellite (*TESS*). *TESS* is deployed in an elliptical, 2:1 lunar synchronous orbit with a period of 13.7 d. Each annual cycle of *TESS* observations are split up into sectors lasting two orbits, or about 27 d. The detector consists of four contiguous CCD cameras, each covering a 24° x 24° field of view (FoV), making up a 24° x 96° strip aligned along ecliptic latitude lines. The data are stored with the short cadence (SC), lasting 120 s and the long cadence (LC), lasting 1800 s. When one sector's observations have been completed, the instrument FoV is shifted eastward by 27°, naturally pivoting around the ecliptic pole. It takes 13 sectors to pivot around one pole, then the FoV is shifted to the other hemisphere for the next cycle. As a result, the regions near the ecliptic poles are observed during every sector and are known as the continuous viewing zones of *TESS*. Luckily, AA Dor is located in this zone around the southern ecliptic pole. We downloaded all available data from the "Barbara A. Mikulski Archive for Space Telescopes" (MAST)[1]. The data span all 13 sectors with the exception of Sector 4, during which AA Dor was not included in the target list. We used the SC data which has a time resolution high enough to allow us to sample the eclipses and to search for stellar pulsations up to 4166 μHz, covering both the g-mode and partially the p-mode regions in an amplitude spectrum. We extracted PDCSAP_FLUX, which is corrected for on-board systematics and neighbors' contribution to the overall flux. We clipped fluxes at 5σ to remove outliers, de-trended long term variations (of the order of days) with polynomials. We show the resultant light curve in Figure 1.

[1] archive.stsci.edu

3 STELLAR PULSATIONS

A few of the sdB primaries in HW Vir systems show stellar pulsations. The examples are NY Vir, 2M 1938+4603 and HW Vir. Therefore, we made an attempt to detect stellar pulsations in AA Dor. The light curve of AA Dor is dominated by eclipses and an irradiation effect. In order to detect any pulsations, which would typically have amplitudes close to the 10 parts per thousand (ppt) level, we had to remove the binary orbital signature from the data. First, we used a Fourier domain to calculate the binary frequency and a sequence of harmonics, which appear as a consequence of a non-sinusoidal shape of the flux variation. Then, we prewhitened the binary frequency along with 93 harmonics, and finally clipped the residuals to remove data points that became outliers after prewhitening. We present the result of these processed data in Figure 2. The light curve no longer shows any binary trend. The amplitude spectrum is fairly smooth with just a few low amplitude frequencies. The highest amplitude peak is at 3952.19 μHz with an amplitude of 0.076 ppt. The signal-to-noise (S/N) of this peak is just short of the S/N = 5 criterion if averaging is used but exceeds it if median is used to determine the noise. To determine its significance, we simulated 10 000 pure-noise time series data sets sampled exactly as the *TESS* data. A false-alarm-probability (FAP) of 0.1% is achieved at 0.0814 ppt level and the FAP at 0.076 ppt is only only 91.1%. We suggest this is too small to be considered an intrinsic signal and conclude that AA Dor is not a pulsator at our detection level.

With an effective temperature of 42,000 K (Rauch 2000a), the AA Dor primary is on the hot end of known sdB pulsators, where most sdB stars are non-pulsators. Exceptions have been the sdO (Woudt et al. 2006) and ω Cen pulsators (Brown et al. 2013). Temperatures between 40,000 and 50,000 K may not allow for observable pulsation amplitudes with currently available time-series data sets. Another reason may be that the amplitudes are diluted by an overestimated flux level. The pulsation amplitudes in other HW Vir system primaries, are around 0.1 ppt. If the AA Dor primary has amplitudes below 0.1 ppt, they will be diluted to lower levels since AA Dor is located in front of a dense stellar environment, namely the Large Magellanic Cloud. In Figure 3 we show a part of the sky around AA Dor with the target mask and the optimal aperture over-

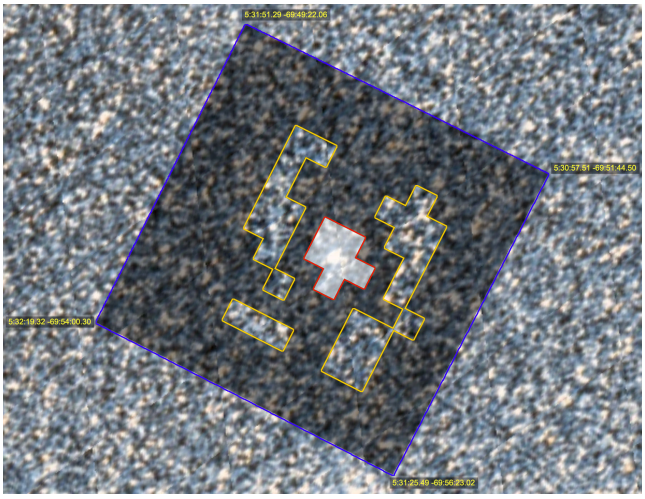

Figure 3. Image showing the part of the sky around AA Dor. The red aperture is used for the target flux, while the yellow one is used for the sky background estimation.

plotted. This figure clearly shows that the CCD pixels used in the optimal aperture for the target overestimate AA Dor 's flux while those used for sky background overestimate the true sky flux. This leads to a dilution in amplitude of any flux variations intrinsic to AA Dor.

4 THE MID-TIMES OF ECLIPSES

Flux variations caused by orbital motion include two eclipses and an irradiation effect. The eclipses are used to study the stability of the orbital period. The mid-times of eclipses are plotted in the so-called *Observed minus Calculated* (O–C) diagram, which can be used to measure an orbital period variation (Sterken 2005). Its variability provides clues on *e.g.* possible mass exchange, a tertiary body, or gravitational wave radiation. To calculate mid-times we used the method described in Kwee & van Woerden (1956). Since we detected no significant pulsations, eclipse shapes are not distorted by other variability and are strictly defined by the geometry of the system. However, to increase the sampling during eclipses and to lower uncertainties of the mid-times, we decided to fold each part of the light curve obtained during a single *TESS* orbit over the binary period calculated from individual eclipses. This folding increases precision of data in an O–C diagram with the price of decreased time resolution, since the total number of eclipses is decreased to 24. However, we do not expect any orbital period variations on time scales of days or less. In addition, we binned data in each eclipse to end up with 30 points per eclipse. We show the result of our light curve folding in Figure 4.

Having folded the light curve, we recalculated the ephemeris from primary eclipses and obtained

$$T_{pri} = 2455681.9153693\,(32)\,\mathrm{BJD} + 0.2615397323\,(40)\,\mathrm{E}$$

Likewise, we re-calculated the ephemeris from secondary eclipses and obtained

$$T_{sec} = 2455682.046202\,(9)\,\mathrm{BJD} + 0.261539724\,(11)\,\mathrm{E}$$

The orbital period derived from both types of eclipses agrees very well to within the errors. We plot the O-C diagrams for primary and secondary eclipses in Figure 5.

Table 1. The orbital period of AA Dor derived since its discovery. The last listed value, generously provided by Dave Kilkenny, has been calculated from eclipses collected between February 1977 and March 2020.

Period [days]	Uncertainty	Reference
0.261539	0.17 sec	Kilkenny et al. (1978)
0.2615398	17 msec	Kilkenny et al. (1979)
0.261539724	0.35 msec	Kilkenny (1983)
0.261539726	0.26 msec	Kilkenny (1986)
0.2615397198	0.15 msec	Kilkenny et al. (1991)
0.261539731	0.17 msec	Kilkenny et al. (2000)
0.2615397363	35 µsec	Kilkenny (2011)
0.2615397323	0.35 msec	this work
0.2615397364	35 µsec	D.Kilkenny (priv. comm.)

The orbital period has been monitored for almost half a century. In Table 1 we list published values of the orbital period. Dave Kilkenny of the South African Astronomical Observatory and his collaborators have been very active in this field. The consecutive values of the orbital period are derived from all mid-times available to the authors. We can see how a longer time baseline helps increase the precision of the orbital period. Kilkenny (2011) presented the most precise orbital period and the O–C analysis, which shows that the orbital period remains very stable over 30 years of monitoring (their Figures 1 and 2). Our work confirms that the orbital period remains stable. The period difference between 1981 and 2019 is 0.69 msec, which gives an upper limit for period change to be $5.75{\cdot}10^{-13}$ s/s. The O–C diagram does not indicate any tertiary body in the system, while other effects, which could cause period change, must be negligible.

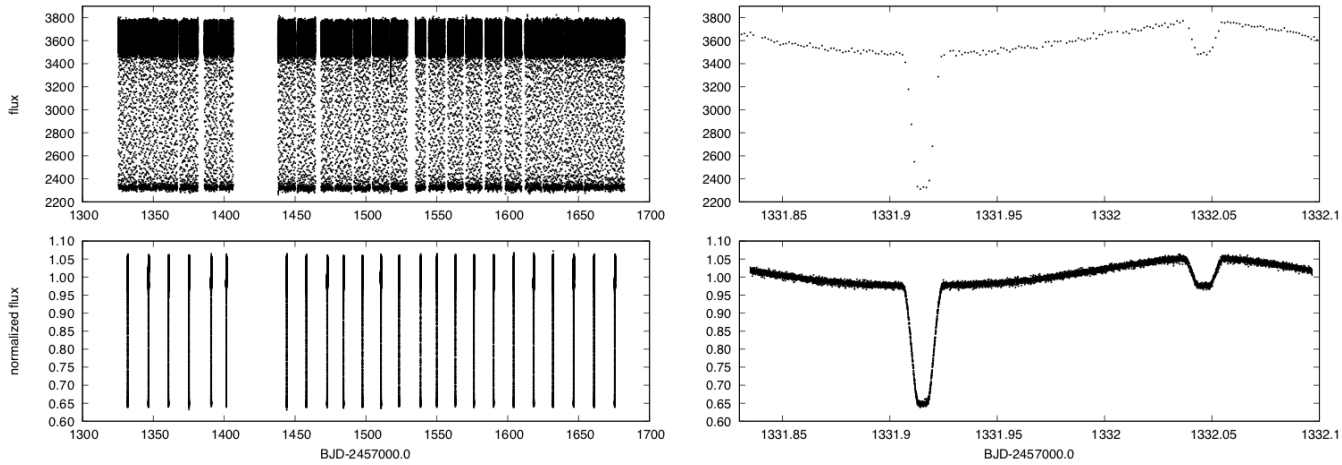

Figure 4. Left upper panel shows the original light curve, while left bottom one shows the light curve folded over the binary orbital period during each *TESS* orbit. The upper right panel shows an unfolded binary orbit, while the bottom right one shows a folded one.

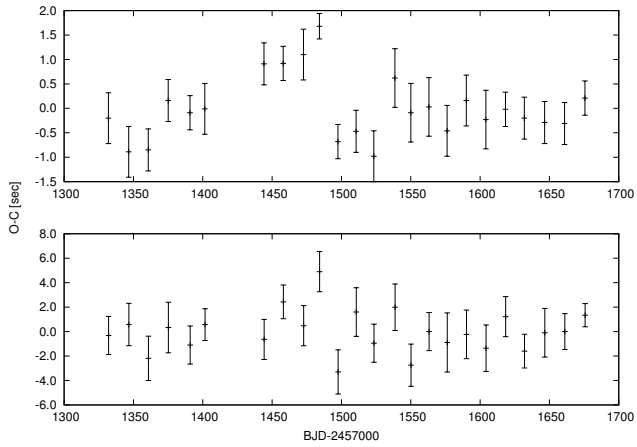

Figure 5. The O-C diagrams for primary (upper panel) and secondary (bottom panel) eclipses.

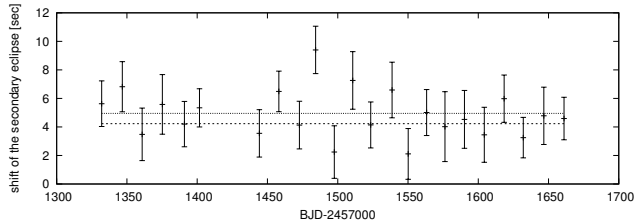

Figure 6. The shift of the secondary eclipse measured in folded and binned eclipses. Two horizontal lines show the range of the mean value of the shift.

5 SHIFT OF THE SECONDARY ECLIPSE

Binary systems with components of unequal masses must have mid-times of secondary eclipses which happen slightly later than half an orbital phase after the primary eclipses. The effect is caused by the finite speed of light and is often called the Rømer delay. This shift must be present unless the masses of both components are equal or the orbit has a specifically-tuned eccentricity which cancels out the shift. In the case of circular orbits, the offset of the secondary eclipse is purely due to the Rømer delay, thus it provides a direct measure of the mass ratio, when the orbital velocity of either component and the orbital period, P, are known. All these quantities can be measured, so the mass estimates are purely observational and do not require any modeling or calibrations. All necessary formulae can be found, *e.g.* in Baran et al. (2018).

We calculated the shifts from 24 folded and binned primary and secondary eclipses. Then we took a mean value, which we found to be 4.59 (36) s. The uncertainty is defined as a standard deviation of the mean value. We plotted our calculated shifts, along with the range of the mean value in Figure 6. Since Hoyer et al. (2015) and Vučković et al. (2016) reported the values of the radial velocity amplitudes of both components, we can calculate the expected shift of the secondary eclipses, assuming the orbit remains circular. Hoyer et al. (2015) cited a value of K_2 to be $232.9^{16.6}_{-6.5}$ km/s and K_1 to be 40.15 (11) km/s. Vučković et al. (2016) cited K_2 to be 231.3 (7) km/s and K_1 to be 39.63 (21) km/s. The uncertainty of K_2 cited by Vučković et al. (2016) is smaller, therefore, for consistency, we adopted values of K_1 and K_2 values and consequently, the mass ratio, from Vučković et al. (2016). We adopted the orbital period from our ephemeris, calculated from folded primary eclipses. Then, the expected shift of the secondary eclipses from pure Rømer delay, *i.e.* assuming circular orbit, equals 4.599 (28) s. This value agrees very well with the one we derived from our observations, measuring the shift directly from the secondary eclipses.

Using K1, P, and our measured Rømer delay, we derive values for the masses of 0.46 (5) $M_\odot$ and 0.079 (9) $M_\odot$ for the primary and the secondary components, respectively. The masses are in agreement with those derived by both Hoyer et al. (2015) and Vučković et al. (2016) and confirm that the primary has a mass close to the canonical value. The orbit of AA Dor is consistent with $e = 0$. If the orbit were eccentric, it would contribute to the shift of secondary eclipses according to Equation 8 in Baran et al. (2018). There are two parameters that are essential, eccentricity e and the argument of pericentre, ω. If the value of e is non-zero and ω is different from $\pi/2$ or $3\pi/2$, the shift we derived from eclipses would be bigger or smaller depending on the sign of $\cos\omega$. While we cannot completely rule out a non-zero eccentricity, if the orbit were eccentric, while $\cos\omega$ is close to zero, the contribution to the shift of

the secondary eclipse would remain negligible, so the shift of the secondary agrees well with the Rømer delay. Unfortunately, a small eccentricity is not detectable in current observations so a definite conclusion cannot be made. Perhaps, an apsidal motion caused by a precession of an eccentric orbit would help to set the limit on eccentricity, however observations do not indicate this to be the case. Convincing observations to measure precise eccentricity are yet to be collected.

6 STELLAR PARAMETERS: RADIUS, MASS, AND LUMINOSITY

A high precision measurement of the parallax of AA Dor ($\varpi = 2.719 \pm 0.059$ mas) is available through the second data release of the Gaia mission which allows us to derive the stellar parameters radius, mass, and luminosity from the atmospheric parameters ($T_{\rm eff}$ and log g from spectroscopy). To this end the angular diameter is derived from the spectral energy distribution (SED), which combined with the parallax yields the stellar radius.

6.1 Angular diameter and interstellar reddening

The angular diameter Θ is a scaling factor from $f(\lambda) = \Theta^2 F(\lambda)/4$, where $f(\lambda)$ and $F(\lambda)$ are the observed and synthetic stellar surface fluxes, respectively. Because of the light contribution originating from the heated hemisphere of the companion, the sdB fluxes can reliably be measured only when the companion is completely eclipsed by the larger subdwarf, that is at secondary eclipse (see e.g. Schaffenroth et al., 2020 MNRAS submitted). Such data are not available for AA Dor. Nevertheless, many photometric measurements are available in different filter systems, covering the optical (APASS (Henden et al. 2015), SkyMapper DR2 (Onken et al. 2019), Tycho (Høg et al. 2000), *Gaia* (Gaia Collaboration et al. 2018)) and infrared (2MASS (Cutri et al. 2003), DENIS (Fouqué et al. 2000), and WISE (Schlafly et al. 2019)) spectral ranges. Johnson and Strömgren colours are also available (Hauck & Mermilliod 1998; Reed 2003).

Many observations of AA Dor in the ultraviolet were made with the *International Ultraviolet Explorer (IUE)*, which were retrieved from the Final Merged Log of IUE Observations through Vizier (`https://cdsarc.unistra.fr/viz-bin/cat/VI/110`) to derive UV-magnitudes from IUE spectra. Three box filters, which cover the spectral ranges 1300–1800Å, 2000–2500Å, and 2500–3000Å are defined (see Heber et al. 2018). We averaged magnitudes derived from 13 SWP and 12 LWR low resolution (6Å) spectra taken through the large (20 arcsec) aperture.

Published photometric measurements are mostly averaged from observations taken at multiple epochs. Hence they are contaminated by some extra light from the companion. Because the amplitude of the reflection effect is larger in the red/infrared spectral range than in the blue and ultraviolet, we expect stronger contamination in the former region.

Another factor that influences the spectral energy distribution is interstellar reddening. Even though interstellar extinction is probably low at high Galactic latitudes, it has to be taken into account. We use the reddening law of Fitzpatrick et al. (2019) and the angular diameter is determined simultaneously with the interstellar colour excess. A χ^2 based fitting routine is used to match synthetic flux distributions from the grid of model atmospheres calculated with ALTLAS12 to the observed magnitudes (see Heber et al. 2018, for details). We use spectroscopic parameters of $T_{\rm eff} = 42{,}000(1000)$ K and log g = 5.46(5) (Klepp & Rauch 2011b) and a helium abundance of $n_{He}/n_{H} = 0.0008(2)$ (Rauch 2000b).

Table 2. Results for a single spectrum fit.

Color excess $E(B-V)$	0.035 ± 0.005 mag
Angular diameter $\log(\Theta\,(\mathrm{rad}))$	-10.571 ± 0.007
Radius $R = \Theta/(2\varpi)$	$0.216 \pm 0.006\ R_\odot$
Mass $M = gR^2/G$	$0.49^{+0.07}_{-0.06}\ M_\odot$
Luminosity $L/L_\odot = (R/R_\odot)^2(T_{\rm eff}/T_{\rm eff,\odot})^4$	130^{+15}_{-14}
Generic excess noise $\delta_{\rm excess}$	0.020 mag

Table 3. Results for a spectrum fit considering an additional black body spectrum representing the light emitted from the heated hemisphere of the companion.

Color excess $E(B-V)$	$0.014^{+0.022}_{-0.014}$ mag
Angular diameter $\log(\Theta\,(\mathrm{rad}))$	$-10.600^{+0.029}_{-0.038}$
Radius $R = \Theta/(2\varpi)$	$0.204^{+0.014}_{-0.019}\ R_\odot$
Mass $M = gR^2/G$	$0.42 \pm 0.09\ M_\odot$
Luminosity $L/L_\odot = (R/R_\odot)^2(T_{\rm eff}/T_{\rm eff,\odot})^4$	112^{+22}_{-21}
Blackbody component:	
Blackbody temperature $T_{\rm bb}$	$12000^{+\ 6000}_{-11900}$ K
Blackbody surface ratio $A_{\rm eff,bb}/A_{\rm eff}$	$0.48^{+0.37}_{-0.24}$
Generic excess noise $\delta_{\rm excess}$	0.018 mag

Table 4. Results for a spectrum fit considering an additional stellar spectrum representing the light emitted from the heated hemisphere of the companion.

Color excess $E(B-V)$	$0.007^{+0.012}_{-0.007}$ mag
Angular diameter $\log(\Theta\,(\mathrm{rad}))$	$-10.610^{+0.018}_{-0.020}$
Component 1:	
Radius $R = \Theta/(2\varpi)$	$0.198 \pm 0.010\ R_\odot$
Mass $M = gR^2/G$	$0.41^{+0.07}_{-0.06}\ M_\odot$
Luminosity $L/L_\odot = (R/R_\odot)^2(T_{\rm eff}/T_{\rm eff,\odot})^4$	108^{+16}_{-14}
Component 2:	
Effective temperature $T_{\rm eff}$	10700^{+3600}_{-1600} K
Surface ratio $A_{\rm eff}/A_{\rm eff,1}$	1.0 ± 0.4
Radius $R = (A_{\rm eff}/A_{\rm eff,1})^{1/2}\Theta/(2\varpi)$	$0.20^{+0.04}_{-0.05}\ R_\odot$
Luminosity $L/L_\odot = (R/R_\odot)^2(T_{\rm eff}/T_{\rm eff,\odot})^4$	$0.23^{+0.54}_{-0.19}$
Generic excess noise $\delta_{\rm excess}$	0.014 mag

We modeled light contamination from the reflection effect on the hemisphere facing the subdwarf using a black body and a stellar spectrum. When adding a black body its temperature and the relative emission area are additional parameters in addition to interstellar reddening and the subdwarf's angular diameter. For the stellar spectrum we used solar composition models from the grid of Husser et al. (2013). The additional fit parameters are the effective temperature of the companion model spectrum as well as the surface ratio. Results are summarized in Tables 2, 3, and 4 and the final fit is displayed in Figs. 7, 8, and 9.

6.2 Stellar radius, mass and luminosity

In order to determine stellar parameters we corrected the Gaia DR2 parallax of AA Dor for the zero point offset of −0.029 (Lindegren

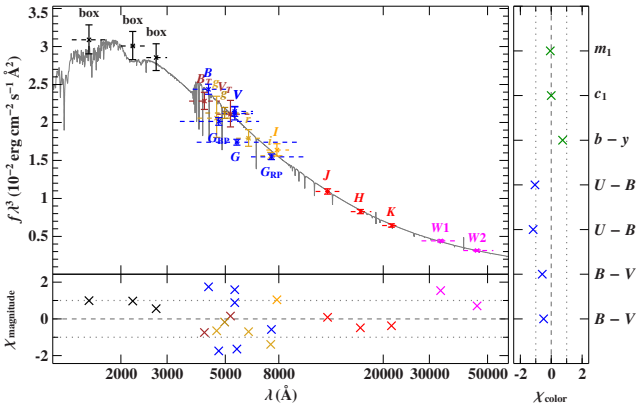

Figure 7. Comparison of synthetic and observed photometry (flux times wavelength to the power of three) and colours: *Top panel, left hand side:* Spectral energy distribution of AA Dor Filter-averaged fluxes converted from observed magnitudes. Dashed horizontal lines depict the approximate width of the respective filters (widths at 10% of maximum). The best-fitting model, smoothed to a spectral resolution of 6 Å, is shown in gray. *Bottom panel:* Residual χ: Difference between synthetic and observed magnitudes divided by the corresponding uncertainties. *right hand panel:* Residual χ for Johnson and Strömgren colours. Difference between synthetic and observed colours divided by the corresponding uncertainties. The different photometric systems are displayed in the following colours: (APASS-griz, golden; SkyMapper DR2-g (golden; Johnson (APASS, blue; ; Johnson (Tycho, brown;) ; *Gaia* (blue; 2MASS (red:); DENIS-I (yellow;); WISE (magenta;). UV magnitudes derived from IUE spectra are labelled "box" (see text). Parameters resulting from the fit are listed in Table 2.

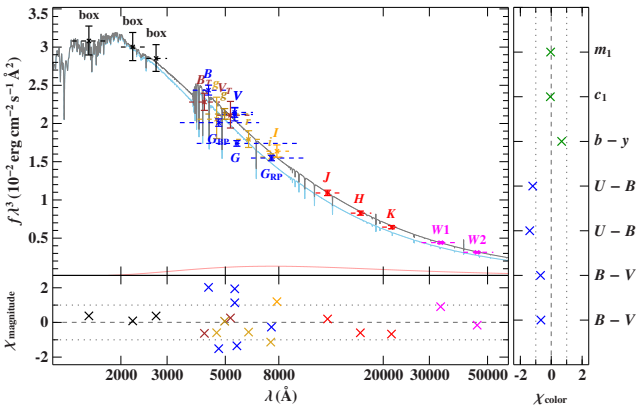

Figure 8. Same as Fig. 7, but adding a black body spectrum representing the companion spectrum. The contribution of the sdOB primary to the best-fit synthetic SED is shown in light blue, while that of the black body in light pink. Model parameters are listed in Table 3.

et al. 2018). From the atmospheric parameters (log g and T_{eff}) and the angular diameter the stellar radius R, mass M, and luminosity L are derived. Their respective uncertainties are derived via Monte Carlo error propagation.

The radius R is derived from parallax and angular diameter. Then the mass follows from the spectroscopic gravity. Finally, the luminosity results from the radius and spectroscopic T_{eff}. For the subdwarf mass, the single spectrum fit gives $M = 0.49\,M_\odot$. When adding a companion spectrum, fits give its T_{eff} close to 10,000 K, irrespective of the type of spectrum used (stellar or black body). Also the emitting surface area on the companion is of the same size

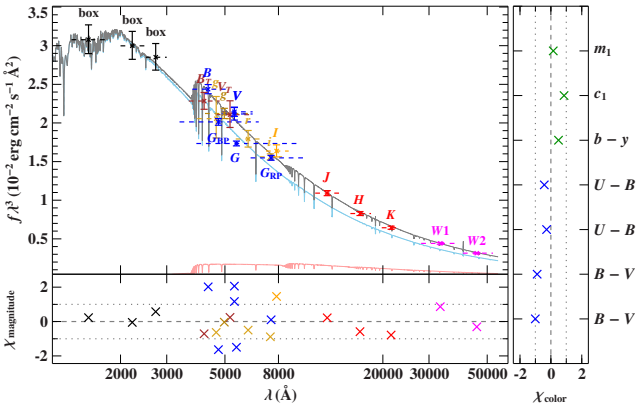

Figure 9. Same as Fig. 8, but representing the emitted spectrum of the companion's heated hemisphere by a stellar model. The contribution of the sdOB primary to the best-fit synthetic SED is shown in light blue, while that of the companion in light pink. Model parameters are listed in Table 4.

for both cases and as large as that of the irradiating hot subdwarf. Note, however, that the uncertainties are large, in particular for the black body solution (see Table 3).

As the generic excess noise is almost identical for all three fits, none can be preferred with respect to the others. The WISE magnitudes are better reproduced by models allowing for companion flux and, because the uncertainties for the parameters of the companion are larger for the black body solution, we adopt the composite stellar spectrum solution. Accordingly, the preferred stellar parameters are $R = 0.199(7)\,R_\odot$, $M = 0.41(6)\,M_\odot$, and $L = 109^{+14}_{-12}\,L_\odot$. The interstellar colour excess is zero.

It should be noted that in all three cases the mass of the sdOB primary is consistent with the canonical evolutionary mass. Because of the high quality of the Gaia parallax, the sdOB radius is very precise, independently of the SED model chosen, and in good agreement with the result of the light curve analysis by Hilditch et al. (2003).

Finally, we placed AA Dor in the Hertzsprung-Russell diagram (Figure 10) to compare its position with canonical evolutionary models from Dorman et al. (1993). For HW Vir, Baran et al. (2018) derived an astrometric radius from its Gaia parallax in a similar way as done here for AA Dor. Using the effective temperature of 28,000 K (Vučković et al. 2014) we derive its astrometric luminosity. The comparison in Figure 10 demonstrates that AA Dor is in an evolved state of evolution beyond core-helium exhaustion, while HW Vir is a bona-fide EHB star. The positions of both stars are consistent with evolutionary models of canonical mass.

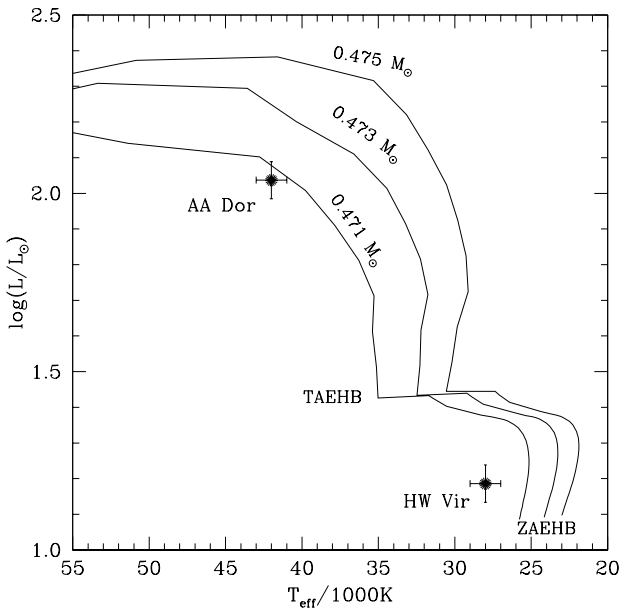

Figure 10. Positions of AA Dor and HW Vir in the Hertzsprung-Russell diagram compared to evolutionary EHB tracks from Dorman et al. (1993) labeled by their stellar masses. The zero-age EHB is indicated as well as the terminal-age EHB (termination of core helium burning).

7 SUMMARY

We have presented new photometric observations of AA Dor collected with the *TESS* satellite. Since AA Dor is located in the southern continuous viewing zone of *TESS*, we obtained a total of 12 sectors of data spanning just over one year. AA Dor is a close binary system consisting of a hot primary and a cool companion. The light curve shows variations caused by mutual eclipsing and an irradiation effect. As in other HW Vir systems, we searched for stellar pulsations in the hot primary, with a null result. The reason may be twofold. The primary is hotter than those in other systems, which does not favor the driving mechanism, and the *TESS* data precision is lower than *Kepler* data, resulting in a higher detection limit.

We have analysed eclipses by deriving their mid-times and calculating an O–C diagram. This analysis confirmed a very stable orbital period with a limit on the period change to be not faster than $5.75 \cdot 10^{-13}$ s/s. Such a value excludes a tertiary body in the system, as well as any significant mass exchange. We have also measured a shift of the secondary eclipse. There are only a few other sdB stars for which the shift of the secondary eclipse has been derived. Baran et al. (2015) reported a shift of 1.76 s for 2M 1938+4603 after it had been observed for three years with the *Kepler* spacecraft, Baran et al. (2018) reported a shift of 1.509 sec for HW Vir based on *K2* data, and another two stars were reported by Schaffenroth et al. (2015) and Lee et al. (2017) using ground-based data, yet neither had sufficient precision to derive a precise shift. The shifts in 2M 1938+4603 and HW Vir under an assumption of circular orbits, are too small to reproduce canonical masses for the primaries. It was suggested that either the mass is truly low and the primaries are low-mass post RGB stars which have not gone through a helium flash, or the shifts are affected by non-zero eccentricity that is too small to be confirmed by current observations. AA Dor is the first case when the shift agrees with the prediction based on a radial velocity amplitude of the cool companion. This amplitude was derived neither for 2M 1938+4603 nor HW Vir.

We searched the public TESS archive for HW Vir candidates by matching targets with the Geier et al. (2017) Gaia-selected subdwarf sample (Table 5). Although these stars are certainly worth closer follow-up, none of them are in the continuous viewing zone, and therefore the length of the *TESS* observations is limited to one or two months. We note that the two new systems with periods longer than that of AA Dor would be particularly welcome targets for Rømer delay measurements, since the delays would be more significant in the wider orbits. TON 301 is an excellent new target for monitoring by the Northern observatories. On the other hand, EC 02406–6908 has a very shallow grazing secondary eclipse, making observations challenging. The folded light curves of nine new HW Vir systems calculated from photometry taken with *TESS* are plotted in Figure 11.

The fundamental stellar parameters (radius, mass, and luminosity) were derived independently through analysis of the spectral energy distribution by making use of the high-precision trigonometric parallax from Gaia. The results of both approaches corroborate that the primary of AA Dor is a canonical mass hot subdwarf, and its effective temperature, radius and luminosity are consistent with an evolutionary state beyond core helium burning. The mass of the secondary companion is close to the limit for nuclear burning.

Table 5. Known HW Vir systems and new candidates observed with *TESS*. Only systems observed with either *TESS* or *K2* in SC mode have been included.

Name	V* name	TIC	P d	K_1 km/s	G mag	Plx mas	Reference
J19447+5449		467187065	0.0642	-	15.78	0.59	Schaffenroth et al. (2019)
KPD 2045+5136		365213081	0.0896	-	15.23	0.95	Schaffenroth et al. (2019)
HE 0516-2311		408187719	0.0912	-	15.93	0.50	Schaffenroth et al. (2019)
PTF1 J011339.09+225739.1		611402948	0.0934	74.2	16.65	0.70	Wolz et al. (2018)
HS 0705+6700	V470 Cam	99641129	0.0956	85.8	14.62	0.81	Drechsel et al. (2001)
SDSS J0820+0008		455206965	0.0962	47.4	15.18	0.66	Geier et al. (2011)
PG 1336–018	NY Vir	175402069	0.1010	78.6	13.39	1.81	Vučković et al. (2007)
J19065+2807		281948821	0.1121	-	15.65	0.54	Schaffenroth et al. (2019)
BD–07°3477	HW Vir	156618553	0.1168	82.3	10.61	5.80	Baran et al. (2018)
EC 10246–2707		193092806	0.1185	71.6	14.44	0.90	Barlow et al. (2013)
2M 1938+4603		271164763	0.1258	65.7	12.14	2.50	Østensen et al. (2010)
EVR-CB-003		396004353	0.1315	-	13.53	1.78	Ratzloff et al. (2020)
ASAS 10232–3737		73764693	0.1393	81.0	11.71	3.74	Schaffenroth et al. (2013)
2M 1533+3759		148785530	0.1618	71.1	12.98	1.90	For et al. (2010)
J21469+6616		322390461	0.1935	-	16.22	0.72	New
FBS 0747+725		441613385	0.2083	-	16.52	0.49	Pribulla et al. (2013)
LB 3459	AA Dor	425064757	0.2615	39.2	11.16	2.72	Vučković et al. (2016)
EC 23068–4801		139266474	0.2641	-	15.39	0.65	Drake et al. (2017)
Ton 301		165797593	0.3697	-	13.80	1.19	Schaffenroth et al. (2019)
EC 02406–6908		259864042	0.4607	-	14.67	0.86	New

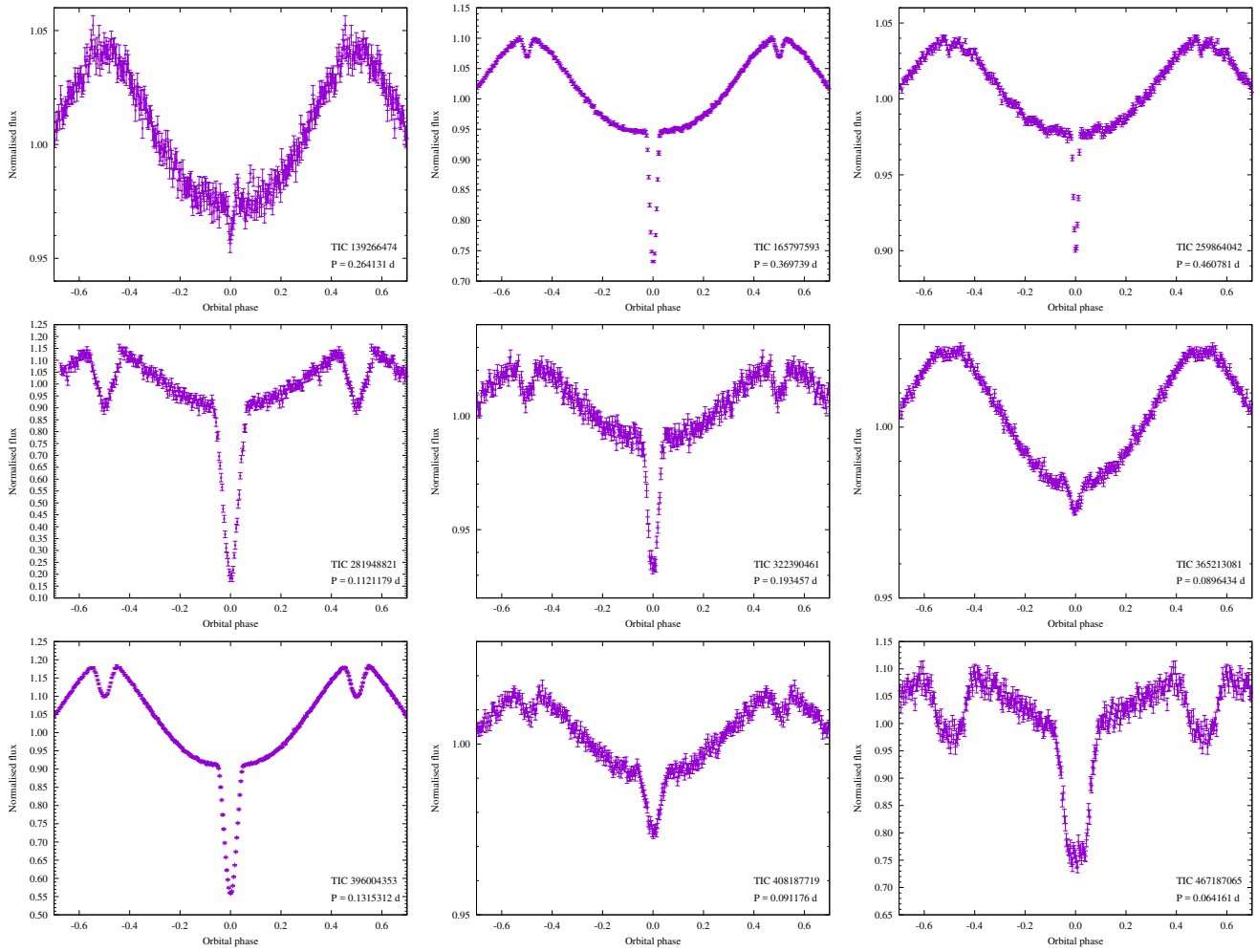

Figure 11. The folded light curves of nine new HW Vir candidate systems we found in *TESS* photometry.

ACKNOWLEDGEMENTS

The authors thank Dave Kilkenny for providing the newest unpublished orbital period estimation included in Table 1, and Kosmas Gazeas and Brad Barlow for useful comments. Financial support from the Polish National Science Centre under projects No. UMO-2017/26/E/ST9/00703 and UMO-2017/25/B/ST9/02218 is appreciated. This work presents results from the European Space Agency (ESA) space mission *Gaia*. *Gaia* data are being processed by the *Gaia* Data Processing and Analysis Consortium (DPAC). Funding for the DPAC is provided by national institutions, in particular the institutions participating in the *Gaia* MultiLateral Agreement (MLA). The *Gaia* mission website is https://www.cosmos.esa.int/gaia. The *Gaia* archive website is https://archives.esac.esa.int/gaia. This research was made possible through the use of the AAVSO Photometric All-Sky Survey (APASS), funded by the Robert Martin Ayers Sciences Fund. This paper includes data collected by the *TESS* mission. Funding for the *TESS* mission is provided by the NASA Explorer Program.

DATA AVAILABILITY

The datasets were derived from MAST in the public domain archive.stsci.edu.

REFERENCES

Almeida L. A., Jablonski F., Tello J., Rodrigues C. V., 2012, MNRAS, 423, 478
Baran A., Zola S., Blokesz A., Østensen R., Silvotti R., 2015, A&A, 577, 146
Baran A., et al., 2018, MNRAS, 481, 2721
Baran A., Telting J., Jeffery C., Østensen R., Vos J., Reed M., Vučković M., 2019, MNRAS, 489, 1556
Barlow B., Wade R., Liss S., 2012, ApJ, 753, 101
Barlow B. N., et al., 2013, MNRAS, 430, 22
Brown T., Landsman W., Randall S., Sweigart A., T. L., 2013, ApJ, 777, 22
Charpinet S., Fontaine G., Brassard P., Chayer P., Rogers F. J., Iglesias C. A., Dorman B., 1997, ApJ, 483, 123
Charpinet S., et al., 2011, A&A, 530, 3
Charpinet S., et al., 2019, A&A, 632, 90
Cutri R. M., et al., 2003, VizieR Online Data Catalog, p. II/246
Dorman B., Rood R. T., O'Connell R. W., 1993, ApJ, 419, 596
Drake A. J., et al., 2017, MNRAS, 469, 3688
Drechsel H., et al., 2001, A&A, 379, 893
Fitzpatrick E. L., Massa D., Gordon K. D., Bohlin R., Clayton G. C., 2019, ApJ, 886, 108
Fontaine G., Brassard P., Charpinet S., Green E. M., Randall S. K., Van Grootel V., 2012, A&A, 539, 12
For B.-Q., et al., 2010, ApJ, 708, 253
Fouqué P., et al., 2000, A&AS, 141, 313
Gaia Collaboration et al., 2018, A&A, 616, A1
Geier S., et al., 2011, ApJ, 731, L22
Geier S., Østensen R. H., Nemeth P., Gentile Fusillo N. P., Gänsicke B. T., Telting J. H., Green E. M., Schaffenroth J., 2017, A&A, 600, A50
Han Z., Podsiadlowski P., Maxted P. F. L., Marsh T. R., Ivanova N., 2002, MNRAS, 336, 449
Hauck B., Mermilliod M., 1998, A&AS, 129, 431
Heber U., 2016, PASP, 128, 2001
Heber U., Irrgang A., Schaffenroth J., 2018, Open Astronomy, 27, 35
Henden A. A., Levine S., Terrell D., Welch D. L., 2015, in American Astronomical Society Meeting Abstracts #225. p. 336.16
Hilditch R. W., Harries T. J., Hill G., 1996, MNRAS, 279, 1380
Hilditch R. W., Kilkenny D., Lynas-Gray A. E., Hill G., 2003, MNRAS, 344, 644
Høg E., et al., 2000, A&A, 355, L27
Hoyer D., Rauch T., Werner K., Hauschildt P., Kruk J., 2015, A&A, 578, 125
Husser T. O., Wende-von Berg S., Dreizler S., Homeier D., Reiners A., Barman T., Hauschildt P. H., 2013, A&A, 553, A6
Kaplan D., 2010, ApJ, 717, 108
Kilkenny D., 1983, SAAOC, 7, 55
Kilkenny D., 1986, The Observatory, 106, 160
Kilkenny D., 2011, MNRAS, 412, 487
Kilkenny D., Hill P. W., 1975, MNRAS, 173, 625
Kilkenny D., Hilditch R., Penfold J., 1978, MNRAS, 183, 523
Kilkenny D., Lynas-Gray A., Hilditch R., 1979, in van Horn H., Weidemann V., eds, White Dwarfs and Variable Degenerate Stars. Proceedings of IAU Colloq. 53. p. 255
Kilkenny D., Harrop-Allin M., Marang F., 1991, IBVS, 3569, 1
Kilkenny D., Koen C., O'Donoghue D., Stobie R. S., 1997, MNRAS, 285, 640
Kilkenny D., Keuris S., Marang F., Roberts G., van Wyk F., Ogloza W., 2000, The Observatory, 120, 48
Klepp S., Rauch T., 2011a, A&A, 531, 7
Klepp S., Rauch T., 2011b, A&A, 531, L7
Kwee K., van Woerden H., 1956, Bulletin of the Astronomical Institutes of the Netherlands, 12, 327
Lee J., Youn J.-H., Hong K., Han W., 2017, ApJ, 839, 39
Lindegren L., et al., 2018, A&A, 616, A2
Menzies J., Marang F., 1986, in Hearnshaw J., Cottrell P., Reidel Dordrecht eds, Instrumentation and Research Programmes for Small Telescopes. Proceedings of the International Astronomical Union Symposium No. 118. p. 305
Onken C. A., et al., 2019, Publ. Astron. Soc. Australia, 36, e033
Østensen R., et al., 2010, MNRAS, 408, 51
Pribulla T., et al., 2013, Information Bulletin on Variable Stars, 6067, 1
Ratzloff J. K., et al., 2020, ApJ, 890, 126
Rauch T., 2000a, A&A, 356, 665
Rauch T., 2000b, A&A, 356, 665
Rauch T., Werner K., 2003, A&A, 400, 271
Reed B. C., 2003, AJ, 125, 2531
Schaffenroth V., Geier S., Drechsel H., Heber U., Wils P., Østensen R. H., Maxted P. F. L., di Scala G., 2013, A&A, 553, A18
Schaffenroth V., Barlow B., Drechsel H., Dunlap B., 2015, A&A, 576, 123

Schaffenroth V., et al., 2019, MNRAS, 630, 80
Schlafly E. F., Meisner A. M., Green G. M., 2019, ApJS, 240, 30
Sterken C., 2005, in Sterken C., ed., Astronomical Society of the Pacific Conference Series Vol. 335, The Light-Time Effect in Astrophysics. p. 3
Vučković M., Østensen R., Bloemen S., Decoster I., Aerts C., 2008, in Heber U., Jeffery C. S., Napiwotzki R., eds, Astronomical Society of the Pacific Conference Series Vol. 392, Hot Subdwarf Stars and Related Objects. p. 199
Vučković M., Bloemen S., Østensen R., 2014, in van Grootel V., Green E., Fontaine G., Charpinet S., eds, Meetings on Hot Subdwarf Stars and Related Objects Vol. 481, ASP Conference Series. p. 259
Vučković M., Østensen R., Németh P., Bloemen S., Pápics P., 2016, A&A, 586, 146
Vučković M., Aerts C., Østensen R., Nelemans G., Hu H., Jeffery C. S., Dhillon V. S., Marsh T. R., 2007, A&A, 471, 605
Wolz M., et al., 2018, Open Astronomy, 27, 80
Woudt P., et al., 2006, MNRAS, 371, 1497